Asian Journal of Chemistry; Vol. 37, No. 4 (2025), 931-942

ASIAN JOURNAL OF CHEMISTRY

https://doi.org/10.14233/ajchem.2025.33600

Influence of Mn and Yb on Structural, Optical, Magnetic Properties, Photocatalytic and Biological Activity of Cobalt Nanoferrites Synthesized by Citrate Gel Method

SURYAM NEERADI[1], RAKESH CHILIVERY[2], ABBU VENUGOPAL[3] and LAXMA REDDY KOTHA[1,*]

[1]Department of Chemistry, Department of Chemistry, Osmania University, Hyderabad-500007, India
[2]Department of Chemistry, B.V. Raju Institute Technology, Narsapur-502313, India
[3]Department of Chemistry (H&S), CVR College of Engineering, Hyderabad-501510, India

*Corresponding author: E-mail: klreddy200542@osmania.ac.in

Received: 1 February 2025; *Accepted*: 24 March 2025; *Published online*: 29 March 2025; AJC-21955

The citrate gel method was used to prepare nanostructured ferrites having composition $Co_{1-y}Mn_yYb_xFe_{2-x}O_4$ ($x = y = 0.00$, 0.02, 0.04, 0.06, 0.08 and 0.1) nanoferrites and investigated their structural, magnetic, catalytic and antibacterial activities. A cubic spinel structure with crystallite diameters between 16.77 nm to 34.84 nm was established by X-ray diffraction (XRD), while granular morphology and elemental composition were disclosed by scanning electron microscopy (SEM) and energy-dispersive X-ray spectroscopy (EDS). Molecular vibrations were described by Fourier-transform infrared (FTIR) and Raman spectroscopy, which verified the production of spinel structures. Vibrating sample magnetometry (VSM) revealed that doping doses caused considerable changes in magnetic anisotropy by varying magnetic characteristics like coercivity and saturation magnetization. Methylene blue and rhodamine blue dyes were used to investigate the photocatalytic activity of these ferrites and YMN-5 showed the best degradation efficiency. Moreover with optimal doping, the antimicrobial activity against a variety of pathogens showed increased efficiency. These results demonstrate the potentiality of Yb-doped Mn-Co ferrites in the biomedical applications and environmental remediation.

Keywords: Cobalt nanoferrites, Ytterbium, Manganese, Optical activity, Catalytical activity, Biological activity.

INTRODUCTION

In material science, nanoferrites are extensively studied for their versatility in applications like catalysis, energy storage, sensors and biomedical technologies [1], because of their unique properties such as super paramagnetism, high surface area and tunable magnetic behaviour at the nanoscale. Their properties can be precisely controlled through synthesis methods and by doping or altering their cation composition. These modifications influence their thermal stability and magnetic performance [2]. A type of ceramic magnetic materials known by the general formula AB_2O_4, spinal ferrites are extensively researched due to their special structural, catalytic and magnetic characteristics. Where, A and B represent distinct cations, such as divalent and trivalent metal ions, respectively, and the spinel crystal arrangement represents the basis of these materials' structure. The cations occupy the interstitial tetrahedral and octahedral positions inside the closely packed cubic lattice of oxygen atoms (O). Although there may be cation inversion depending on the conditions of the material's creation, (A) ions typically occupy tetrahedral sites in a typical spinel ferrite, whereas (B) ions occupy octahedral sites [3].

Doping nanoferrites with rare earth or *f*-block elements, such as La, Yb, Nb or Sm, significantly enhances their functional properties by introducing unique electronic configurations and localized magnetic moments. These dopants improve saturation magnetization, coercivity and thermal stability, making the materials ideal for applications in high-density magnetic storage and spintronic devices [4,5]. Moreover, the rare earth ions develop defect states within the bandgap, boosting the photocatalytic efficiency and visible-light absorption for environmental pollutant degradation [6]. The ionic radii of rare-earth cations are bigger than those of Fe^{3+} or Co^{2+} [7]. They produce strain and cause lattice deformation when they replace these ions in the spinel lattice. This strain results from changes in bond angles and lengths caused by the bigger ions upsetting the lattice's normal organization. The density, elastic qualities and crystallinity of the material can all be impacted by such distortions.

The magnetic anisotropy and coercivity of the spinel materials are changed by the induced strain, which also affects the magnetic interactions between cations at tetrahedral and octahedral sites. The *d*-electrons of the transition metal ions in the spinel structure interact with the unpaired *f*-electrons that rare-earth ions supply. The total magnetic moment of the material is altered by this interaction [8-10]. The magnetic characteristics, including saturation magnetization, coercivity and Curie temperature, can be customized according on the particular rare-earth ion utilized. For example, increased anisotropy from the replacement may result in increased coercivity, which would make the material appropriate for high-density magnetic storage. Because of these benefits, the citrate gel approach is the method of choice for creating nanoferrites with specific characteristics for use in biomedical, catalytic and magnetic applications [11,12].

The nanoferrites also stand out for their magnetic separability and multifunctional applications [13,14]. Magnetic nanoferrites, like $ZnFe_2O_4$ or $CoFe_2O_4$, can adsorb heavy metals or degrade organic pollutants through photocatalysis while being easily removed from treated water using an external magnetic field [15]. Rare earth-doped nanoferrites further enhance the photocatalytic activity by improving visible-light absorption and reducing electron-hole recombination, making them effective in breaking down stubborn pollutants. These materials not only improve treatment efficiency but also offer sustainable and reusable solutions, crucial for addressing global water quality challenges. In this work, the Yb and Mn doped Co nanoferrites were prepared by citrate gel auto-combustion method having composition $Co_{1-y}Mn_yYb_xFe_{2-x}O_4$ ($x = y = 0.00, 0.02, 0.04, 0.06, 0.08$ and 0.1). The effects on the structural, optical, magnetic, photocatalytic and biological activities of varying the Yb and Mn concentrations during the synthesis of cobalt nanoferrites were studied.

EXPERIMENTAL

Synthesis of nanoferrites: The $Co_{1-y}Mn_yYb_xFe_{2-x}O_4$ spinel ferrite nanoparticles ($x = y = 0.00, 0.02, 0.04, 0.06, 0.08$ and 0.1) were synthesized by citrate gel auto-combustion method. In brief, the nanoferrites were produced by dissolving stoichiometric amounts of metal nitrates, such as ytterbium nitrate, manganese nitrate, ferric nitrate and citric acid, in deionized water. Ammonia solution was used to regulate the pH of the stock solution. The dark green colouration of solution indicated neutrality, as the pH was maintained at 7. The gel was synthesized through continuous agitation on a magnetic stirring plate at 80 ºC. After self-ignition, the gel underwent a transformation into porous ferrite powder, and the resulting reaction product was subsequently calcinated in a muffle furnace. The heating process was conducted at 500 ºC for 4 h. The ferrite powder residue underwent grinding for 30 min with a mortar and pestle [16,17].

Characterization: To ascertain the spinel-phase and cubic nature of $Co_{1-y}Mn_yYb_xFe_{2-x}O_4$ ($x = y = 0.00$ YbMN-0; 0.02 = YbMN-1; 0.04 = YbMN-2; 0.06 = YbMN-3; 0.08 = YbMN-4 and 0.1 = YbMN-5) nanoparticles, the X-ray diffraction was performed using a Bruker D-8 advanced and an X-ray diffractometer with Cu*K*α radiation at 0.15406 nm. Energy dispersive spectroscopy (EDS) (JEOL JSM-6480LV) and a field emission scanning electron microscope (FE-SEM, JEOL JSM-6480LV) were used to analyze the morphology. A laser FTIR (Perkin-Elmer L1600) can be used to confirm the spinel phase development of the materials. Utilizing a Shimadzu UV-NIR UV-3600i Plus double beam spectrophotometer, the spectral band gaps of Mn & Yb-substituted $CoFe_2O_4$ were measured. The magnetism of prepared sample was evaluated using a vibrating sample magnetometry (VSM) (VSM-Quantum Design, USA, PPMS-DynaCool-9T).

Photocatalytic activity: The methylene blue (MB) and rhodamine blue (RB) dyes, which were influenced by visible light, demonstrated the photocatalytic activity of the synthesized nanoferrites samples. The process comprised the preparation of 0.05 g of MB and RB dyes, along with the individual dissolution of 0.05 g of catalysts (nanoferrite sample) in double distilled water. A magnetic stirrer was employed for thoroughly mixing the dye and catalyst followed by the addition of 50 mL of double distilled water. The mixture was kept in the dark for 20 min and then 400 W power bulb was utilized to produce the irradiation light. A 20-gauge syringe was utilized to collect the irradiation samples at the predetermined time intervals, specifically set at 20 min.

RESULTS AND DISCUSSION

XRD studies: The XRD patterns of the synthesized cobalt nanoferrities $Co_{1-y}Mn_yYb_xFe_{2-x}O_4$ ($x = y = 0.0, 0.02, 0.04, 0.06, 0.08$ and 0.1) nanoferrites are shown in Fig. 1. Different crystallographic planes are represented by separate peaks in the X-ray diffraction (XRD) patterns, including (111), (220), (311), (222), (400), (422), (511) and (440). The crystalline phase and structural characteristics of the prepared Co-Mn-Yb nanoferrites are validated by the X-ray diffraction (XRD) spectra. According to the JCPDS card 001-1121, the measured diffraction peaks are accurately indexed to the cubic spinel structure [18]. The synthesized materials crystallize in the *Fd*3*m* space group, which is a property of the cubic spinel structure and this group is frequently linked to a face-centered cubic (FCC) layout, emphasizing the symmetry and stability of the nano-ferrites materials. The absence of impurities or secondary phases in the XRD patterns confirms the efficient synthesis of Co-Mn-Yb nanoferrite particles. The calculated crystallite sizes range from 16.77 nm to 34.84 nm and the broadening of the peaks indicates the formation of the nanocrystalline particles. The Debye-Scherrer's equation was used to determine the crystalline size of the nanoferrites [19].

$$\text{Crystalline size (D)} = \frac{0.94\lambda}{\beta\cos\theta}$$

The lattice parameter of the samples was calculated by following equation:

$$\text{Lattice parameter a} = d\sqrt{h^2 + k^2 + l^2}$$

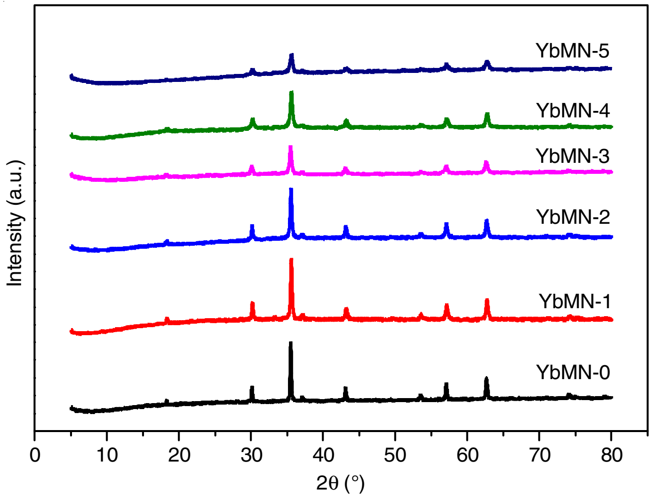

Fig. 1. X-ray diffraction patterns of $Co_{1-y}Mn_yYb_xFe_{2-x}O_4$ ($x = y$ = 0.0, 0.02, 0.04, 0.06, 0.08 and 0.1) nanoferrites

where d indicates interplanar distance and h, k and *l* indicates the miller indices. The average crystalline size and lattice parameter of $Co_{1-y}Mn_yYb_xFe_{2-x}O_4$ nanoferrites with x = 0.0, 0.02, 0.04, 0.06, 0.08 and 0.1 vary, as shown in Fig. 2. The average crystalline size decreases 16.77 nm from about 34.84 nm. The lattice parameter of the pure sample was found to be 8.364 Å. It gradually decreases with further modifications, but for the YbMN-4 sample, it was found to be the highest 8.378 Å. This variation shows that the structural modifications like ionic substitution, lattice strain or synthesis have changed the unit cell size (Table-1). Both characteristics may change if metal cations with various ionic radii are substituted.

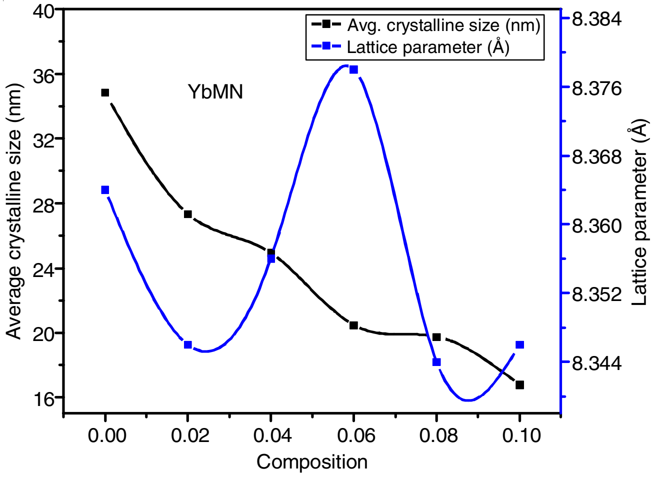

Fig. 2. Variation of crystalline size and lattice parameter of $Co_{1-y}Mn_yYb_xFe_{2-x}O_4$ ($x = y$ = 0.0, 0.02, 0.04, 0.06, 0.08 and 0.1) nanoferrites

The computed unit cell volume was ranged from 580 to 588 Å, which indicate the slight changes due to the addition of Yb to the host material. Strain effects, minor crystal lattice distortions or the substitutional insertion of Yb and Mn can all cause these differences in the lattice parameters and unit cell volume. The change in X-ray density and unit cell volume for a set of samples is shown in Fig. 3. The X-ray density shows an inverse trend and rapidly decreasing at the sites where the unit cell volume is maximized (Table-1).

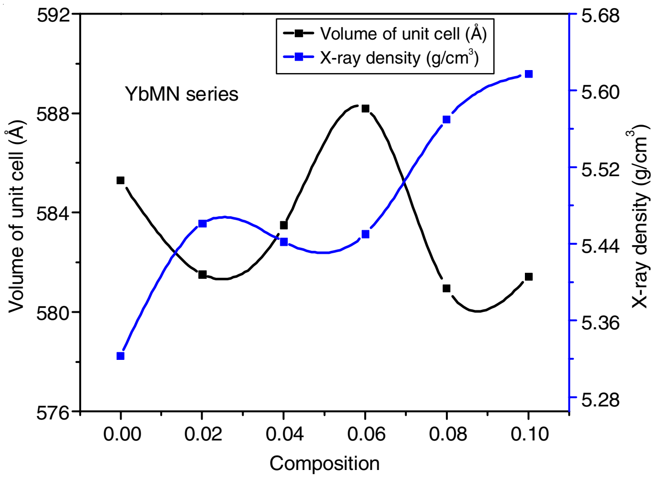

Fig. 3. Volume of unit cell and X-ray density of $Co_{1-y}Mn_yYb_xFe_{2-x}O_4$ ($x = y$ = 0.0, 0.02, 0.04, 0.06, 0.08 and 0.1) nanoferrites

Morphological studies: The FE-SEM images of prepared $Co_{1-y}Mn_yYb_xFe_{2-x}O_4$ nanoferrites with $x = y$ = 0.0, 0.02, 0.04, 0.06, 0.08 and 0.1 show granularly structured particles that clearly cluster in all samples (Fig. 4). The particles are homogeneous and smaller at low doping concentrations (x = 0.0 and 0.02), suggesting the regulated nucleation and growth during synthesis. However, the larger particles and improved agglomeration as the doping concentration increases (x = 0.08 and 0.1). The observed behaviour is attributed to grain growth and enhanced interparticle magnetic interactions commonly found in doped nanoferrites. Furthermore, denser clusters and some obvious gaps or pores occur as the degree of agglomeration seems to increase with increasing Yb and Mn content [20]. These morphological modifications imply that the dopants have an impact on the surface energy and crystal lattice structure, which in turn affects the kinetics of particle formation. To comprehend the material qualities, these observations are essential.

Fig. 5 shows the EDS spectrum of $Co_{1-y}Mn_yYb_xFe_{2-x}O_4$ x = 0.0, 0.02, 0.04, 0.06, 0.08 and 0.1 nanoferrites. The EDS analysis confirmed the presence of the major elements, such as

TABLE-1
XRD PARAMETERS OF $Co_{1-y}Mn_yYb_xFe_{2-x}O_4$ x = 0.0, 0.02, 0.04, 0.06, 0.08 AND 0.1 NANOFERRITES

Name of the composition	Peak position (2θ) (°)	FWHM (β)	Average crystalline size (nm)	Lattice parameter (Å)	Volume of unit cell (Å)	X-ray density (g/mm^3)
YbMN-0	35.503	0.2268	34.84	8.364	585.30	5.323
YbMN-1	35.582	0.2889	27.34	8.346	581.52	5.461
YbMN-2	35.539	0.3169	24.93	8.356	583.49	5.442
YbMN-3	35.441	0.3860	20.47	8.378	588.19	5.450
YbMN-4	35.593	0.3997	19.76	8.344	580.97	5.570
YbMN-5	35.584	0.4710	16.77	8.346	581.41	5.617

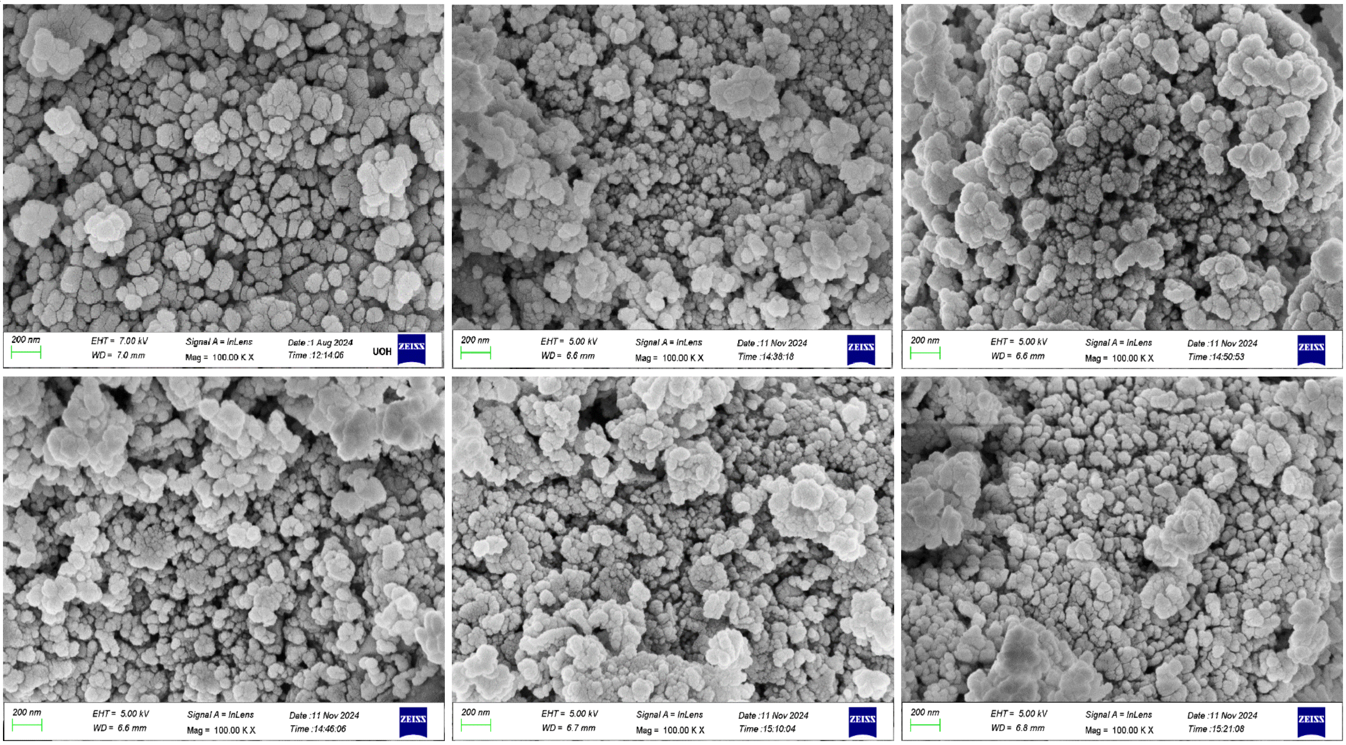

Fig. 4. FE-SEM images of $Co_{1-y}Mn_yYb_xFe_{2-x}O_4$ ($x = y = 0.0, 0.02, 0.04, 0.06, 0.08$ and 0.1) nanoferrites

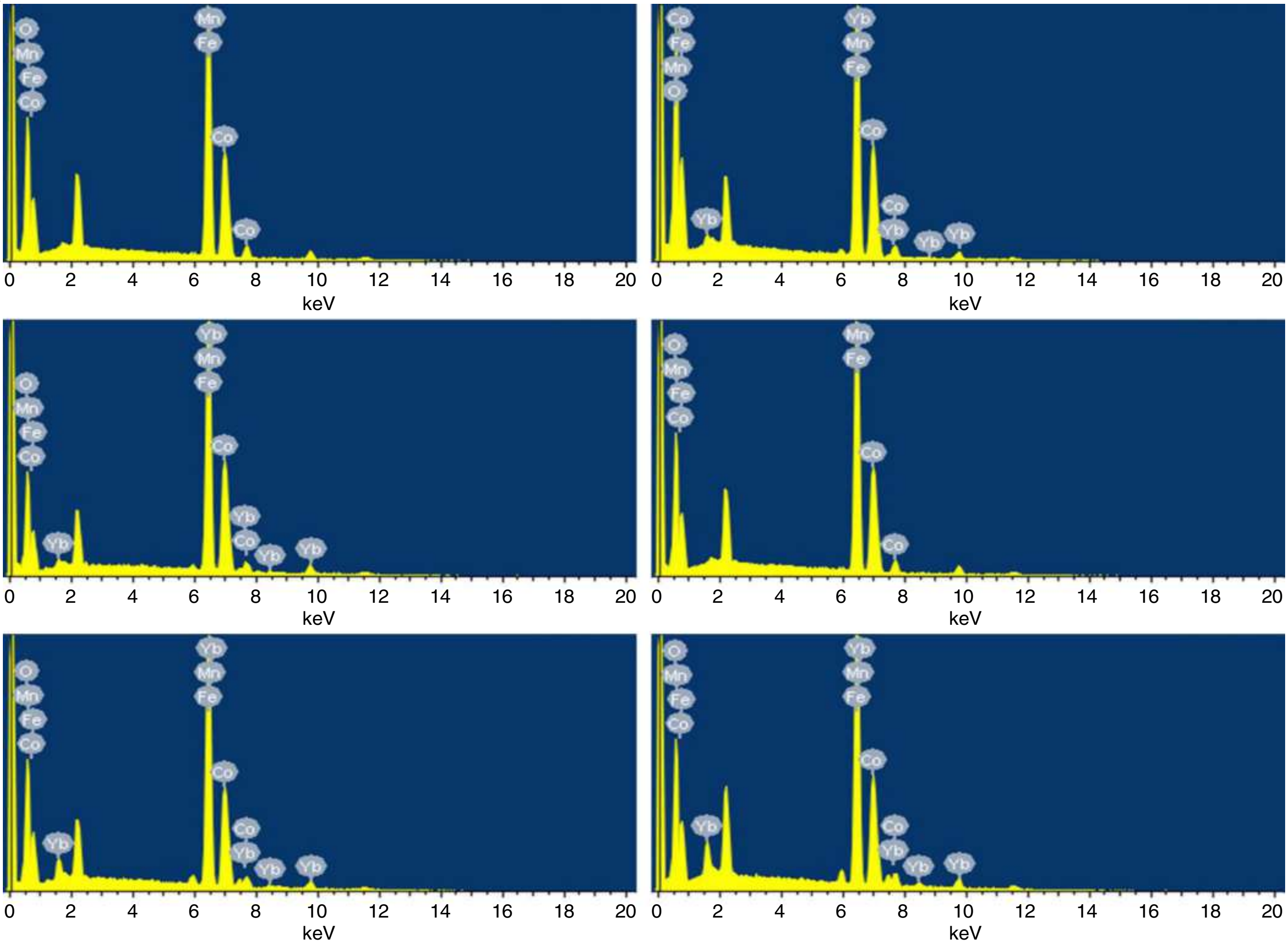

Fig. 5. EDS spectra of $Co_{1-y}Mn_yYb_xFe_{2-x}O_4$ ($x = y = 0.0, 0.02, 0.04, 0.06, 0.08$ and 0.1) nanoferrites

TABLE-2
EDX ANALYSIS OF $Co_{1-y}Mn_yYb_xFe_{2-x}O_4$ x = 0.0, 0.02, 0.04, 0.06, 0.08 AND 0.1 NANOFERRITES

Composition	Co (%)		Mn (%)		Yb (%)		Fe (%)		O (%)	
	Atomic	Weight	Atomic	Weight	Atomic	Weight	Atomic	Weight	Atomic	Weight
YbMN-0	18.16	27.32	0	0	0	0	38.57	55.00	43.27	17.67
YbMN-1	14.67	24.47	0.41	0.64	0.39	1.92	30.88	48.73	53.62	24.24
YbMN-2	19.99	27.47	0.60	0.76	0.96	3.88	41.59	54.15	36.85	13.74
YbMN-3	16.01	24.66	0.89	1.28	1.20	5.43	32.99	48.17	48.91	20.46
YbMN-4	24.29	16.91	1.36	1.02	6.28	1.49	51.34	37.70	42.89	16.73
YbMN-5	17.14	24.47	1.24	1.54	2.52	1.53	51.39	37.98	27.71	34.48

Fe and Co, along with dopants like Yb and Mn and found to be consistent with the stoichiometric ratio (Table-2).

FTIR studies: The FTIR spectra of prepared nanoferrites with x, y = 0.0, 0.02, 0.04, 0.06, 0.08 and 0.1 are displayed in Fig. 6. The vibrations associated with the tetrahedral and octahedral sites in the spinel ferrite structure are represented by distinctive peaks in the low wavenumber region (800-400 cm^{-1}) of the FTIR spectrum. In the tetrahedral sites, the vibrational modes associated with the stretching of metal-oxygen bonds often occur in the higher range of the low wavenumber area, roughly 600-500 cm^{-1}. The interaction between the oxygen atoms and the cations (such as Co, Yb and Fe) which are occupying the tetrahedral spaces is indicated by these peaks. The vibrational modes of the metal-oxygen bonds in the octahedral sites can be identified in the lower range, which is usually between 500 and 400 cm^{-1} [21,22]. The bonding of oxygen with cations located in the octahedral gaps is represented by these peaks. The formation of a spinel ferrite structure with cations dispersed between tetrahedral (A) and octahedral (B) voids is confirmed by the different peaks within this range.

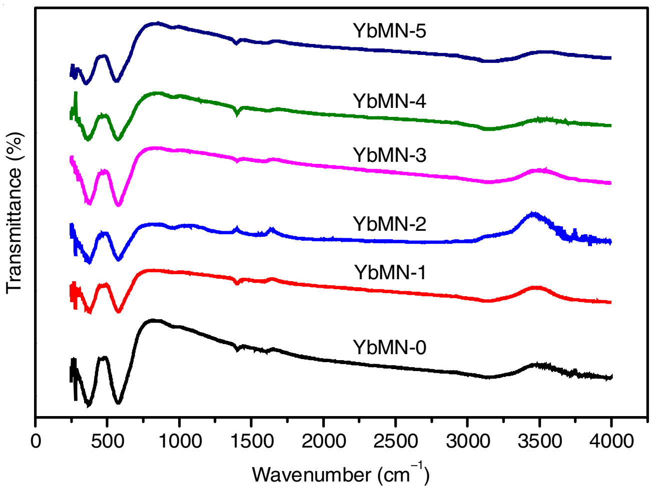

Fig. 6. FTIR spectra of $Co_{1-y}Mn_yYb_xFe_{2-x}O_4$ (x = y = 0.0, 0.02, 0.04, 0.06, 0.08 and 0.1) nanoferrites

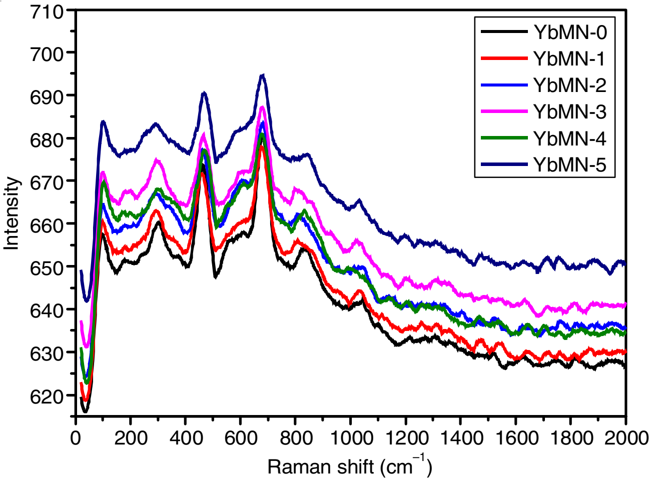

Fig. 7. Raman merged spectra of $Co_{1-y}Mn_yYb_xFe_{2-x}O_4$ (x = y = 0.0, 0.02, 0.04, 0.06, 0.08 and 0.1) nanoferrites

Raman studies: The stretching and bending of metal-oxygen bonds in tetrahedral and octahedral sites correspond to the characteristic Raman-active vibrational modes of nanoferrites, which often exhibit spinel structures [23]. It can also detect secondary phases or contaminants and differentiate between various ferrite phases. Raman spectrum of Yb-Mn-Co nanoferrites (Fig. 7) demonstrates prominent peaks in the low-wavenumber region, indicative of vibrational modes associated with the lattice dynamics of spinel ferrites. These peaks correspond to the stretching and bending vibrations of metal-oxygen bonds, typically observed in spinel structures. The peaks near 800-200 cm^{-1} can be attributed to the symmetric stretching of tetrahedral (A-site) metal ions and asymmetric bending of octahedral (B-site) metal ions. The observed variations in the intensity and slight shifts across the Yb-Mn-Co nanoferrites suggest changes in the local structural symmetry or cation distribution due to varying compositions. The spinel structure belongs to the $Fd3m$ space group, where the irreducible representations predict Raman-active modes as A_{1g}, E_g and T_{2g}. The visible peaks correspond to these Raman-active modes, reflecting the vibrational dynamics of the tetrahedral and octahedral sites. Substitution of Yb, Mn and Co likely alters the cation occupancy and bond lengths, affecting the lattice symmetry and shifting vibrational frequencies. Fig. 8a-f show the Raman deconvoluted spectrum of the synthesized Yb-Mn-Co nanoferrites.The deconvolution of Raman spectra into individual peaks (green curves) allows the identification of various vibrational modes associated with the spinel ferrite structure. In the low-wavenumber region (700-200 cm^{-1}), the intense peaks correspond to the symmetric and asymmetric stretching vibrations of metal-oxygen bonds at the tetrahedral sites (A_{1g}) and bending vibrations at the octahedral sites (T_{2g}) [24,25]. Peaks at higher wavenumbers, though less intense, may be attributed to secondary vibrational modes or lattice disorder-induced effects. The fitting curves (red lines) closely follow the experimental data (black lines), confirming the accuracy of the fitting process and the suitability of the chosen model.

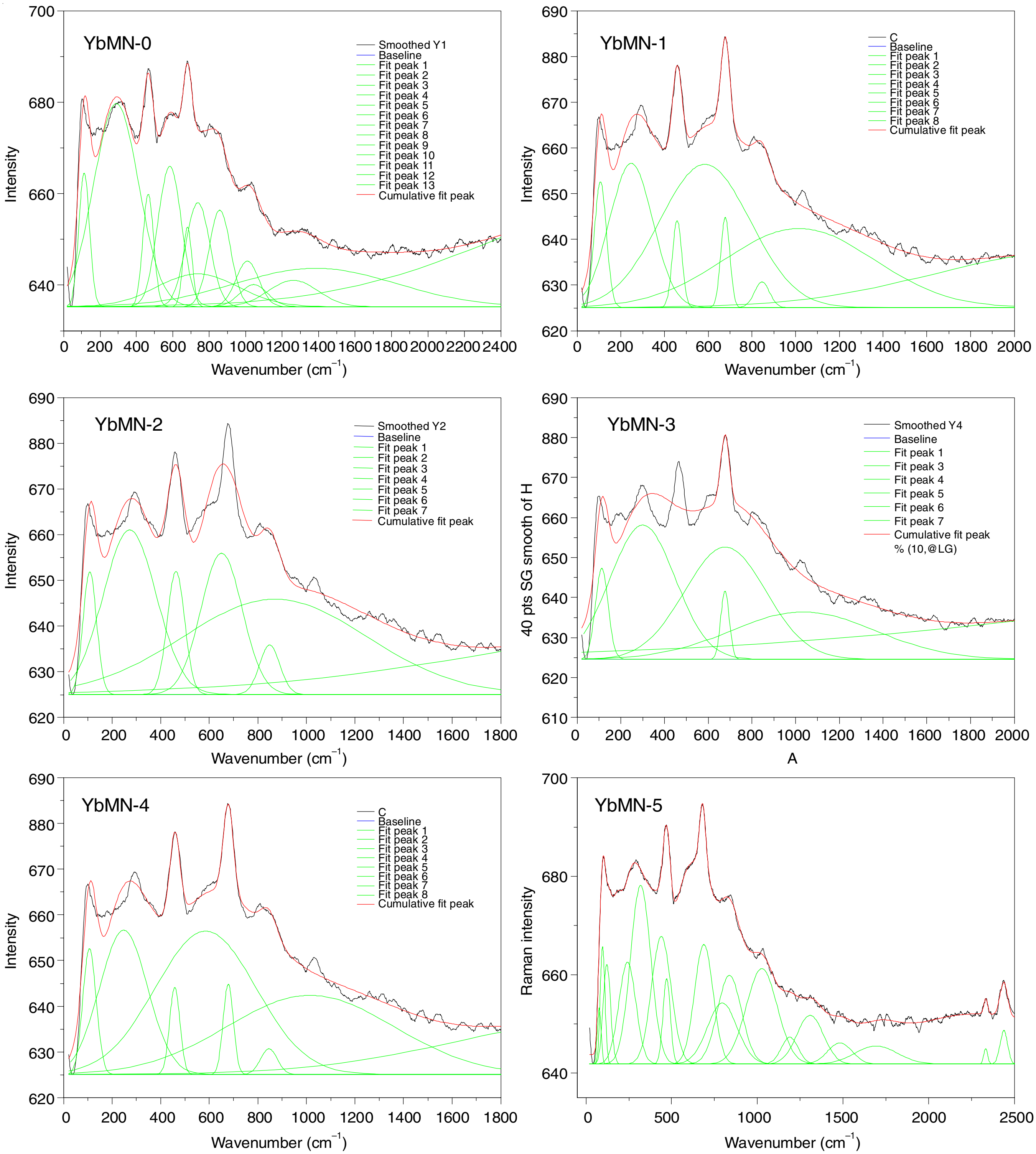

Fig. 8. Raman deconvoluted spectra of $Co_{1-y}Mn_yYb_xFe_{2-x}O_4$ ($x = y = 0.0, 0.02, 0.04, 0.06, 0.08$ and 0.1) nanoferrites

Optical studies: The absorbance-based analysis was done with the help of Tauc's and Urbach's relations [26]. The optical absorption coefficient 'α' wass determined as a function of thickness and absorbance data. Using the following relation, the 'α' have been determined as:

$$\alpha = 2.303 \times \frac{\text{Absorbance}}{\text{Thickness of the sample}}$$

Fig. 9 illustrates the correlation between absorbance and the wavelength of UV light incident on the prepared Yb & Mn doped cobalt nanoferrites and the cut-off edge varies with dopant concentration. For pure sample YbMn-0, the cut-off found to be the highest (539 nm) among the series of samples with different concentrations of the dopant (Table-3). It might occurs due to the changes in the structure of the nanoferrites with a replacement of dopant into base matrix. The rare earth metals

TABLE-3
OPTICAL PARAMETERS OF $Co_{1-y}Mn_yYb_xFe_{2-x}O_4$ x = 0.0, 0.02, 0.04, 0.06, 0.08 AND 0.1 NANOFERRITES

Sample code	Cut-off wavelength (nm)	Indirect band gap (eV)	Direct band gap (eV)	Urbach energy (eV)	Refractive index (n)	Dielectric constant
YbMN-0	539	2.25	2.23	0.72	2.42	5.85
YbMN-1	537	2.28	2.30	0.78	2.45	6.00
YbMN-2	536	2.35	2.38	0.85	2.48	6.15
YbMN-3	533	2.39	2.42	0.90	2.53	6.40
YbMN-4	531	2.44	2.49	0.93	2.58	6.65
YbMN-5	528	2.50	2.56	0.98	2.62	6.86

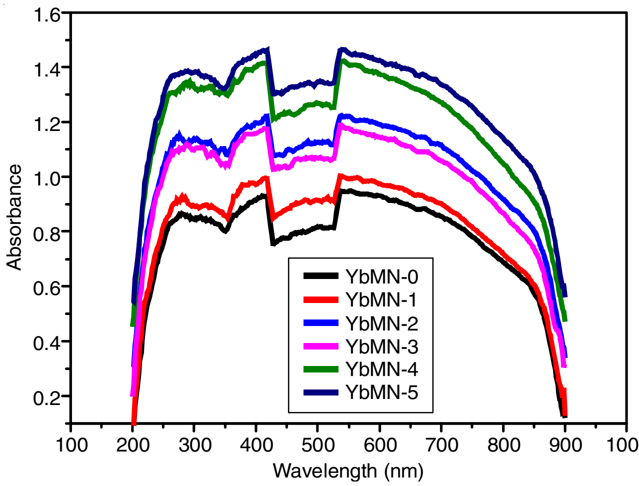

Fig. 9. UV-optical spectra of ytterbium doped cobalt-manganese nanoferrites

like La, Tm, Yb, *etc*. prefers to enter into the octahedral sites and sometimes occupies both the O_h and T_h sites of the base ferrite. The cut-off wavelength is fluctuated between 539-528 nm with a decreasing trend.

The Tauc's plot is a reliable way for determining the indirect and direct band gaps of materials compared to alternative approaches. Fig. 10a depicts the variation of $(\alpha h\nu)^{0.5}$ with the incident energy of photon. The series of Yb-Mn-Co nanoferrites have shown the band gap ($E_{indirect}$) value as 2.25 eV. Moreover, doping of Yb into the base matrix, it increased in a systematic manner. The highest value recorded was 2.50 eV for the YbMn-5 sample, potentially resulting from the transformation of structural variations as Yb content was increased. The Tauc's relation for both direct and indirect bandgaps is represented as follows [27]:

$$(\alpha h\nu)^{1/k} = C(h\nu - E_g)$$

Fig. 10b reflects the variation of $(\alpha h\nu)^2$ with the incident energy of photon. The series of Yb-Mn-Co nanoferrites of the present study have shown the band gap (E_{direct}) value as 2.23 eV. Further, doping of Yb into the base matrix, it increased in a systematic manner and found to the highest as 2.56 eV for YbMN-5 sample (Table-3). It may be due to the conversion of structural fluctuations because of the presence of Yb content [28].

Urbach energy (E_{Urbach}) calculation: One of the parameters linked to the randomness of material is Urbach energy, which is dependent on the absorption coefficient and may be expressed as follows:

$$\ln(\alpha) = \ln(\alpha_o) + \left(\frac{h\nu}{E_{Urbach}}\right)$$

Fig. 11 reflects the variation of absorption coefficient with photon energy which leads to derive the Urbach energy value. In present approach, it varied linearly as a function of dopant concentration from 0 to 0.1 with a step of 0.02. The variation of ΔE found between 0.72 eV to 0.98 V, which gives an additional information that the dopants develops more randomness in the structure of base ferrite composition (Table-3).

Refractive index (μ): The refractive index evaluated from the Tauc's relation using direct band gap energy value. The refractive index of the Yb-Mn-Co nanoferrites increased with

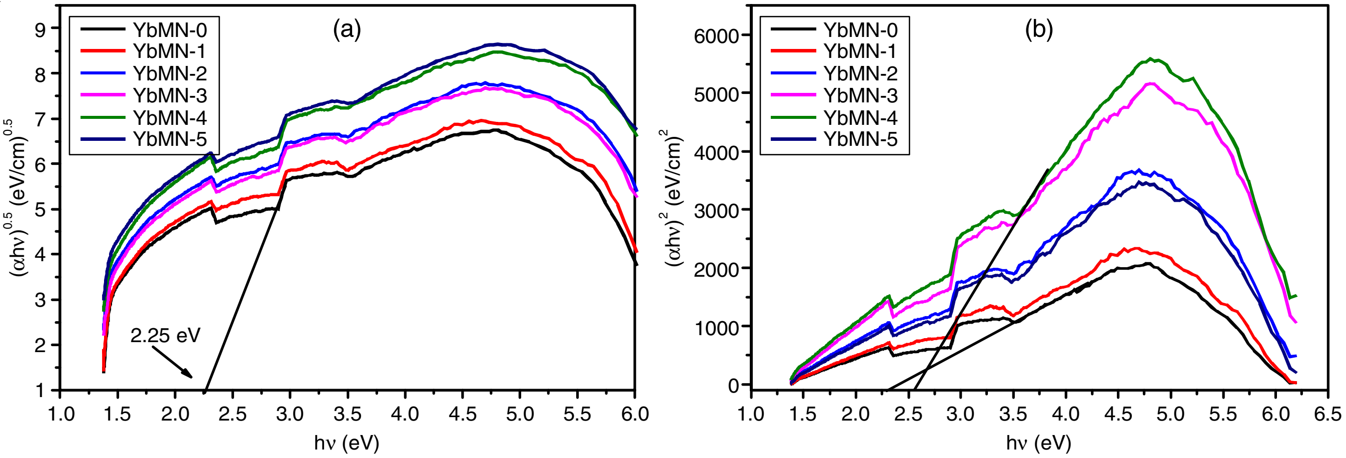

Fig. 10. Taucs relation for (a) indirect and (b) direct energy band gap of ytterbium doped Co-Mn nanoferrites

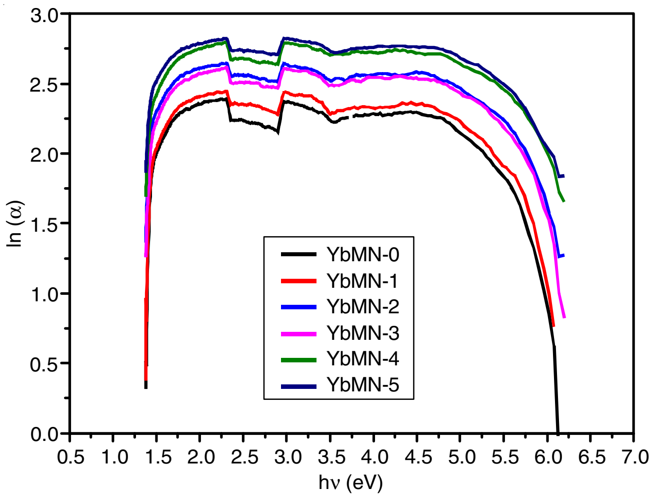

Fig. 11. Urbach energy (E_{Urbach}) calculation of ytterbium doped Co-Mn nanoferrites

the dopant linearly and varied between 2.42-2.62 as the linear increment found (Table-3). The optical dielectric constant is the square of refractive index. It observed to be in the range of 5.85 to 6.86 with an increasing manner (Table-3).

Extinction coefficient (k): In the fabrication and design of optical devices, an evaluation is required about the reflection, transmission, or absorption of light at a specific wavelength. Fig. 12 shows the variations in the k value with wavelength and clearly indicate that the k value increasing at a wavelength around 540nm. The increasing trends of the k values reflects the suitability and efficacy of the Yb-Mn-Co nanoferrites for the optical device applications.

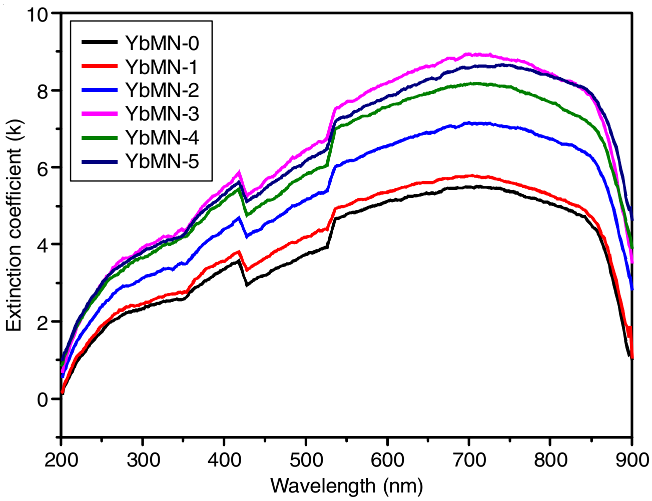

Fig. 12. Extinction coefficient variation with wavelength of Yb doped Co-Mn nanoferrites

Magnetic properties: The VSM hysteresis loops exhibit the typical ferromagnetic behaviour, characterized by clear saturation magnetization (M_s), remanent magnetization (M_r) and coercive field (H_c). The decreasing trend in M_s across samples indicates a reduction in magnetic properties or ferromagnetic phase content (Table-4), whereas alterations in loop breadth signify variances in coercivity, potentially arising from the differences in domain wall pinning or crystal anisotropy [29]. The hysteresis loops of Yb-Mn-Co nanoferrites are shown in Fig. 13. It is observed that M_s decreases with increasing Yb^{3+} substitution. This trend is attributed to the replacement of magnetic Fe^{3+} ions with weakly magnetic or non-magnetic Yb^{3+} ions, which reduces the net magnetic moment. The substitution also weakens the super exchange interactions between Fe^{3+} ions at the tetrahedral (A) and octahedral (B) sites, further lowering the saturation magnetization. Similarly, M_r follows a decreasing trend, as it is directly related to the material's ability to retain magnetization, which diminishes with reduced magnetic ion content. The squareness ratio (M_r/M_s) remains relatively consistent, with minor fluctuations around 0.4 (Table-4). This indicates that the material retains its multi-domain structure throughout the substitution range, characteristic of soft magnetic materials [30,31]. On the other hand, coercivity (H_c) initially increases with Yb^{3+} substitution, reaching a maximum at $x = 0.08$ and then slightly decreases for $x = 0.1$.

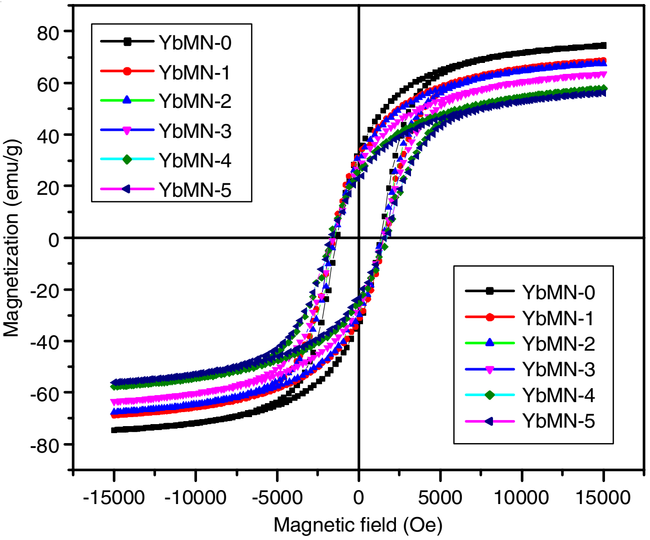

Fig. 13. Hysteresis loops of $Co_{1-y}Mn_yYb_xFe_{2-x}O_4$ ($x = y = 0.0, 0.02, 0.04, 0.06, 0.08$ and 0.1) nanoferrites

TABLE-4
MAGNETIC PARAMETERS (M_s, M_r, H AND M_r/M_s) OF $Co_{1-y}Mn_yYb_xFe_{2-x}O_4$ x = 0.0, 0.02, 0.04, 0.06, 0.08 AND 0.1 NANOFERRITES

Composition	Saturation magnetization, M_s (emu/g)	Remanence magnetization, M_r (emu/g)	Squareness ration M_r/M_s (emu/g)	Coercivity, H_c (Oe)
YbMN-0	74.48	32.99	0.4429	1341
YbMN-1	68.70	32.066	0.4667	1515
YbMN-2	67.59	30.885	0.4569	1446
YbMN-3	63.61	27.47	0.4318	1504
YbMN-4	57.96	25.86	0.4461	1721
YbMN-5	56.11	23.17	0.4129	1593

The initial increase in H_c can be explained by enhanced magnetocrystalline anisotropy introduced by Yb^{3+} ions, making it more difficult to reverse magnetization. However, at higher substitution levels, the dilution of the magnetic lattice weakens magnetic coupling, resulting in a slight reduction in coercivity. These trends indicate potential tunability of magnetic properties, making the materials suitable for applications such as magnetic storage or sensors. Further quantitative analysis could provide more insights into the exact influence of structural or compositional changes on their magnetic performance.

Photoctalytic activity: The removal of organic dyes from wastewater depends heavily on the photocatalytic activity, particularly when nanoferrites are used as catalysts. The efficacy of the photocatalytic process is increased by the increased contact with dye molecules made possible by the high surface area of nanostructured ferrites. Moreover, the magnetic separation facilitates the integration of ferrites into a photocatalytic system, enhancing the reusability of catalyst and also reduces the treatment costs. The efficient photocatalytic degradation as observed in Fig. 14 shows the significant decrease in absorbance with longer exposure times to visible light. Pure YbMN-0 sample shows highest degradation efficiency of methylene blue. Degradation activity of nanosamples depends on various factor like irradiation light, time, surface area and band gap energy of the samples [32].

Fig. 15 shows the photocatalytic activity of rhodamine blue (RB) dye of Yb-Mn-Co nanoferrites. The absorbance spectra were plotted against wavelength, highlighting the primary RB peak around 554 nm. In each subplot, the absorbance intensity decreases progressively with increasing irradiation time, indicating the breakdown of RB molecule due to the photocatalytic activity. Among the samples, YbMN-1 exhibits a more pronounced reduction in absorbance over time, suggesting superior photocatalytic efficiency, likely due to favourable material properties such as a lower bandgap, enhanced charge separation, or a higher surface area. In contrast, YbMN-0, YbMN-1, YbMN-3 and YbMN-5 nanoferrites show relatively slower degradation, with minimal reduction during the initial dark phase, confirming that light activation is critical for the photocatalytic process. Among the samples, YbMN-1 exhibits the highest degradation efficiency, reaching approximately 25% at 120 min, outperforming the other samples. This suggests that YbMN-1 may possess superior photocatalytic properties due to factors such as optimized composition, surface area or band gap energy

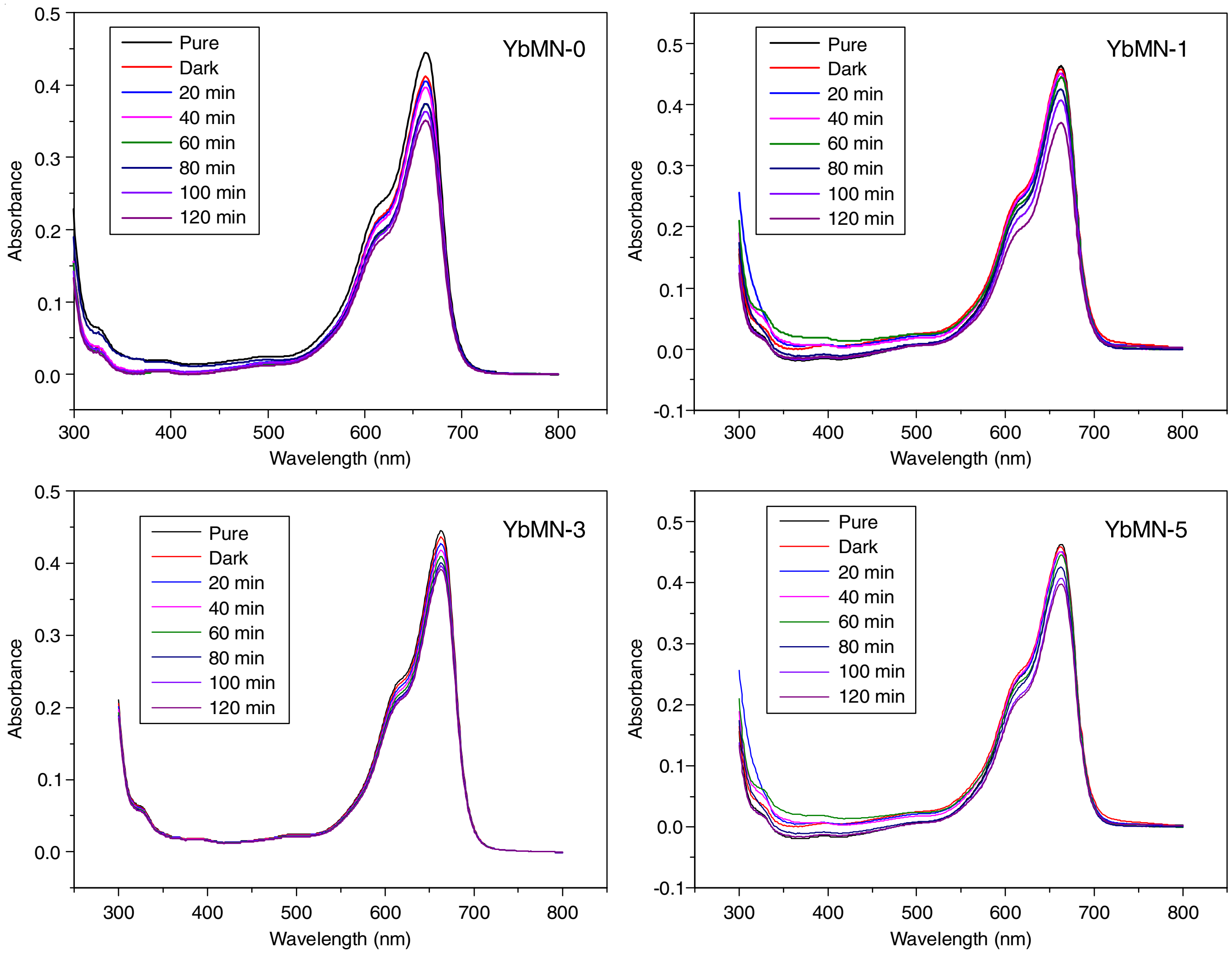

Fig. 14. Photocatalytic activity of $Co_{1-y}Mn_yY_xFe_{2-x}O_4$ ($x = y = 0.0$, 0.02, 0.06 and 0.1) nanoferrites towards methylene blue dye

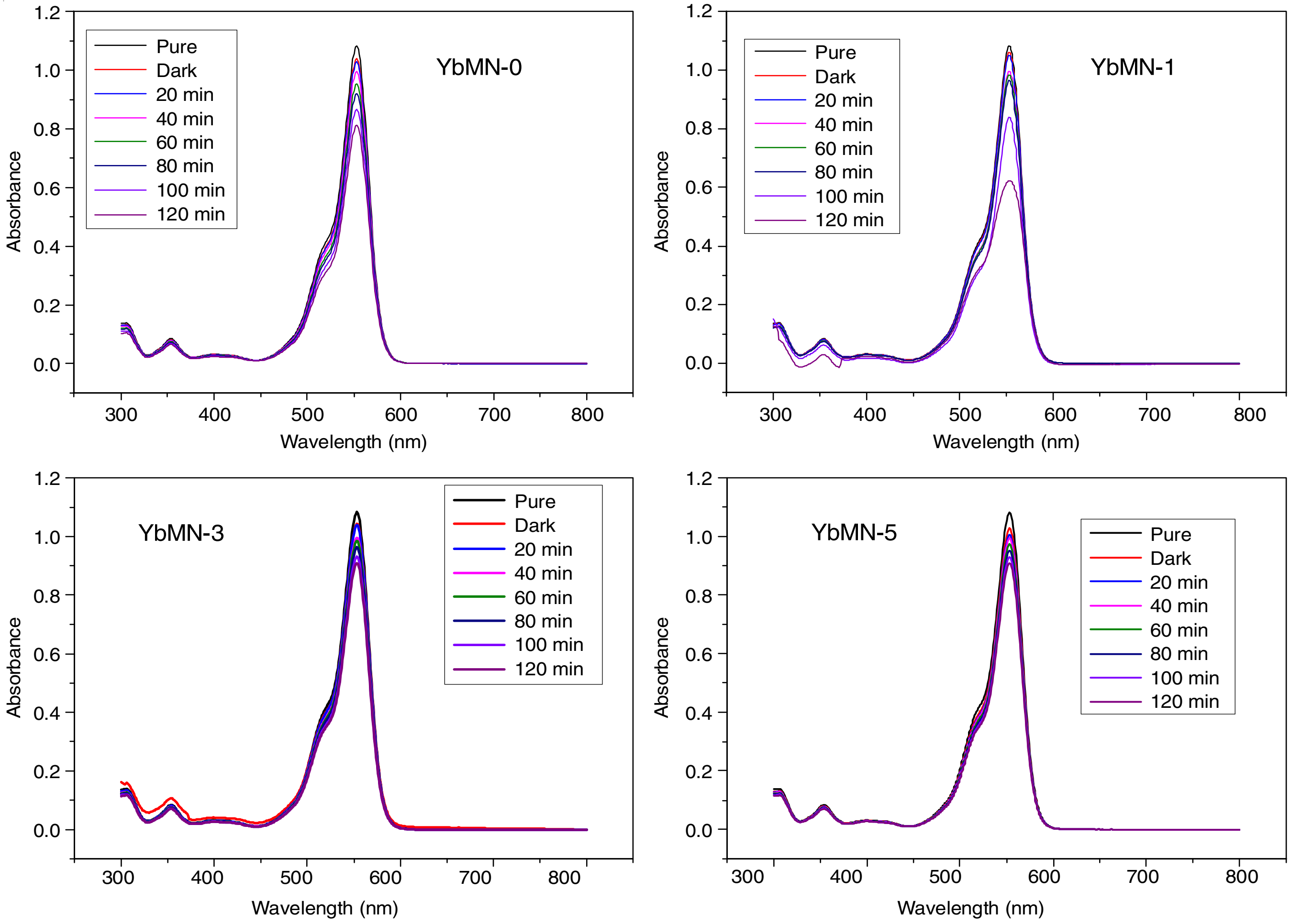

Fig. 15. Photocatalytic activity of $Co_{1-y}Mn_yYb_xFe_{2-x}O_4$ ($x = y = 0.0$, 0.02, 0.06 and 0.1) nanoferrites towards rhodamine blue dye

[33]. The remaining samples show relatively similar trends, with slightly lower efficiencies, highlighting the influence of material composition on photocatalytic performance.

Mechanism: As shown in Fig. 16, the process of photocatalytic activity of nanoferrites consists of multiple phases [34]. The electrons (e^-) in the valence band of the Co-Ni-La nanoferrites are excited by photons when exposed to visible light energy, which causes them to move to the conduction band. Electron-hole pairs are produced by this process e^-/h^+. While the corresponding holes stay in the valence band, the excited electrons gather in the conduction band. The photocatalytic process may become less efficient due to the possibility of electron and hole recombination. However, the recombination is reduced by appropriate nanoferrite design and doping. The electrons in the conduction band contribute to the reduction of the system's oxygen (O_2) molecules, creating reactive oxygen species (ROS) like superoxide anions (O_2^-). The breakdown of organic contaminants depends on these ROS, whereas the hydroxyl radicals ($^{\bullet}OH$) oxidize the organic pollutants and convert them into innocuous byproducts like CO_2 and H_2O. The photocatalytic effectiveness of the material under visible light is largely dependent on its bandgap energy (E_g). Thus, the Yb-Mn-Co nanoferrites are efficient photocatalysts for the environmental applications such as wastewater treatment due to their customized electronic structure, which maximizes charge separation and ROS formation.

Antibacterial activity: The antibacterial activity of the produced Yb & Mn doped Co nanoferrites was examined using two Gram-positive (*Bacillus* and *Staphylococcus*) and two Gram-negative (*E. coli* and *Pseudomonas*) bacterial agents [35]. Among the tested nanoferrites, YbMN-5 showed the highest antibacterial activity against *Bacilli* (14 mm), *E. coli* (13 mm), *Pseudomonas* (10 mm) and *Staphylococcus* (11 mm), approaching the efficacy of the antibiotic control (Table-5). This

TABLE-5
ANTIBACTERIAL ZONE OF INHIBITION VALUES AGAINST GRAM-POSITIVE AND GRAM-NEGATIVE BACTERIA OF $Co_{1-y}Mn_yYb_xFe_{2-x}O_4$ $x = 0.0$, 0.02, 0.06 AND 0.1 NANOFERRITES AGAINST *Staphylococcus*, *Bacillus*, *E. coli* AND *Pseudomonas*

	YbMN-0	YbMN-1	YbMN-3	YbMN-5	Antibiotic
Bacilli	3 mm	6 mm	10 mm	14 mm	17 mm
E. coli	7 mm	8 mm	10 mm	13 mm	18 mm
Pseudomonas	4 mm	6 mm	7 mm	10 mm	16 mm
Staphylococcus	3 mm	5 mm	6 mm	11 mm	16 mm

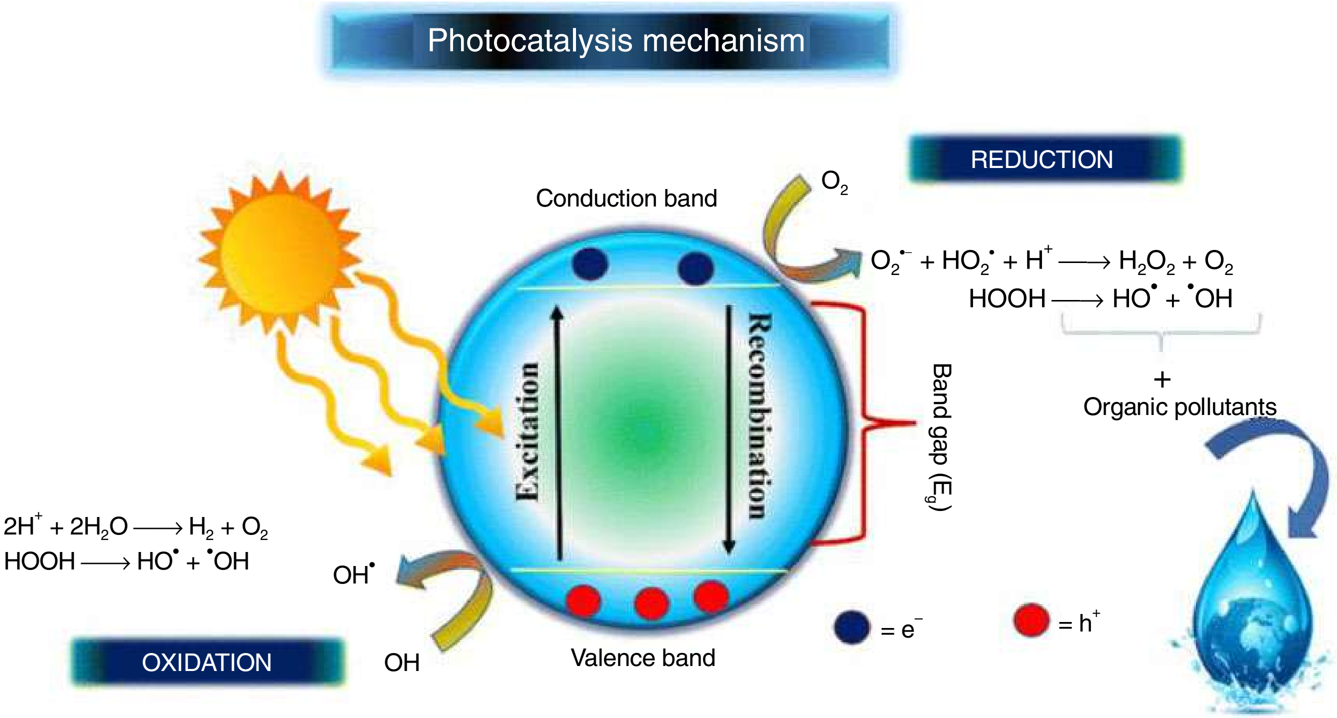

Fig. 16. Mechanism of photocatalytic activity

enhanced activity can be attributed to the substitution of Yb ions in the ferrite structure, which likely improves the surface charge, particle size and surface area. These factors enhance the interaction of Yb-Mn-Co nanoferrites with bacterial cell membranes, leading to higher ROS generation and membrane damage [36]. Other nanoferrites, such as YbMN-3, showed moderate inhibition, while YbMN-0 (control ferrite) exhibited the least activity, indicating a clear enhancement in antibacterial performance with increased Yb content. The results indicate that the composition and concentration of Yb in nanoferrites significantly enhance antibacterial activity, with YbMN-5 demonstrating the most effective results against both Gram-positive and Gram-negative bacteria.

Antifungal activity: Because of the destructive effects that *Sclerotium rolfsii* and *Phytophthora infestans* have on agriculture, the antifungal efficacy of nanoferrites against these diseases is extremely important. The antifungal activity of nanoferrites was evaluated against *P. infestans* and *S. rolfsii*, with inhibition zones compared to a standard antibiotic. Among the tested samples, YbMN-5 exhibited the highest activity against *P. infestans* with a zone of inhibition of 62.2%, significantly outperforming the other nanoferrites but still lower than the antibiotic, which showed 71.5% inhibition. YbMN-1 outperformed the other nanoferrites against S. rolfsii, inhibiting it at 44.22%, slightly less than the standard (46.12%). The control sample (YbMN-0) displayed moderate inhibition for both fungi, serving as a baseline for comparison (Table-6). These results highlight the potential of nanoferrites, particularly YbMN-5, for antifungal applications. However, the variations in activity across samples suggest the need for further optimization to enhance efficacy and achieve results comparable to conventional antibiotics [37].

TABLE-6
ANTIFUNGAL ZONE OF INHIBITION VALUES AGAINST
Phytophthora infestans AND *Sclerotium rolfsii*

Composition	*Phytophthora infestans*	*Sclerotium rolfsii*
YbMN-0	41.7%	33.33%
YbMN-1	32.2%	44.22%
YbMN-3	33.3%	40.00%
YbMN-5	62.2%	43.22%
Antibiotic	71.5%	46.12%

Conclusion

Ytterbium (Yb) and manganese (Mn) doped cobalt nanoferrites having composition $Co_{1-y}Mn_yYb_xFe_{2-x}O_4$ ($x = y = 0.00$, 0.02, 0.04, 0.06, 0.08 and 0.1) were effectively synthesized by citrate gel auto-combustion technique. Single phase and cubic spinel structure were confirmed from X-ray diffraction technique. The crystalline size of the samples were ranged from 16.77 nm to 34.84 nm. The lattice parameter of pure sample found to be 8.364 Å. It gradually decreases as increasing dopant content, but for YbMN-4 sample, it was found to be the highest 8.378 Å. Tetrahedral and octahedral spinel structure confirmed by Raman and FTIR spectroscopy. The development of a cubic spinel phase with improved magnetic and catalytic capabilities as a result of doping was validated by structural analysis. Under visible light, photocatalytic activity showed that dyes may be effectively degraded, with YbMN-0 exhibiting the best results against the methylene blue dye. The antimicrobial activities of the Yb-Mn-Co nanoferrites showed that they are effective against the studied the bacterial strains, making them attractive options for biomedical and environmental treatments. These findings highlight the adaptability of nanostructured nanoferrites and their promise for longterm, scalable uses in antibacterial and wastewater treatment technologies.

ACKNOWLEDGEMENTS

The authors are thankful to Department of Chemistry, University College of Science, Osmania University, Hyderabad, India for providing the necessary facilities to carryout the research work.

CONFLICT OF INTEREST

The authors declare that there is no conflict of interests regarding the publication of this article.

REFERENCES

1. M.B. Mohamed and M. Yehia, *J. Alloys Compd.*, **615**, 181 (2014); https://doi.org/10.1016/j.jallcom.2014.06.156
2. L.V. Hublikar, S.V. Ganachari and V.B. Patil, *Environ. Sci. Pollut. Res. Int.*, **30**, 66994 (2023); https://doi.org/10.1007/s11356-023-27201-z
3. Y. Mouhib and M. Belaiche, *Appl. Phys., A Mater. Sci. Process.*, **127**, 613 (2021); https://doi.org/10.1007/s00339-021-04758-5
4. H. Aglan, I.A. Ali, B.M. Ali and S.A. Kandil, *J. Mater. Sci. Mater. Med.*, **36**, 17 (2025); https://doi.org/10.1007/s10856-025-06859-6
5. A. Hameed, A. Asghar, S. Shabbir, I. Ahmed, A.K. Tareen, K. Khan, G. Hussain, M.Y. Awaji and H. Anwar, *Front. Chem.*, **12**, 1433004 (2024); https://doi.org/10.3389/fchem.2024.1433004
6. L. Saviano, A.A. Brouziotis, E.G.P. Suarez, A. Siciliano, M. Guida, M. Spampinato, M. Trifuoggi, D.D. Bianco, M. Carotenuto, V.R. Spica, G. Lofrano and G. Libralato, *Molecules*, **28**, 6185 (2023); https://doi.org/10.3390/molecules28176185
7. V.S. Kumbhar, A.D. Jagadale, N.M. Shinde and C.D. Lokhande, *Appl. Surf. Sci.*, **259**, 39 (2012); https://doi.org/10.1016/j.apsusc.2012.06.034
8. S. Dabagh, K. Chaudhary, Z. Haider and J. Ali, *Results Phys.*, **8**, 93 (2018); https://doi.org/10.1016/j.rinp.2017.11.033
9. E. Abouzir, M. Elansary, M. Belaiche and H. Jaziri, *RSC Adv.*, **10**, 11244 (2020); https://doi.org/10.1039/D0RA01841D
10. K. Vijaya Babu, G. Satyanarayana, B. Sailaja, G.V. Santosh Kumar, K. Jalaiah and M. Ravi, *Results Phys.*, **9**, 55 (2018); https://doi.org/10.1016/j.rinp.2018.01.048
11. M. Amiri, K. Eskandari and M. Salavati-Niasari, *Adv. Colloid Interface Sci.*, **271**, 101982 (2019); https://doi.org/10.1016/j.cis.2019.07.003
12. H. Qin, Y. He, P. Xu, D. Huang, Z. Wang, H. Wang, Z. Wang, Y. Zhao, Q. Tian and C. Wang, *Adv. Colloid Interface Sci.*, **294**, 102486 (2021); https://doi.org/10.1016/j.cis.2021.102486
13. P.D. Sanasi, D. Santhipriya, Y. Ramesh, M.R. Kumar, B. Swathi and K.J. Rao, *J. Chem. Sci.*, **126**, 1715 (2014); https://doi.org/10.1007/s12039-014-0729-2
14. N. Abbas, N. Rubab, K.H. Kim, R. Chaudhry, S. Manzoor, N. Raza, M. Tariq, J. Lee and S. Manzoor, *J. Colloid Interface Sci.*, **594**, 902 (2021); https://doi.org/10.1016/j.jcis.2021.03.094
15. D.R. Kumar, C.A. Lincoln, D. Ravinder and S.I. Ahmad, *Appl. Phys., A Mater. Sci. Process.*, **126**, 705 (2020); https://doi.org/10.1007/s00339-020-03894-8
16. M.H. Abdellatif and A.A. Azab, *Silicon*, **10**, 1991 (2018); https://doi.org/10.1007/s12633-017-9711-1
17. C.H. Vinuthna, K.C. Babu Naidu, C.C. Sekhar and R. Dachepalli, *Int. J. Appl. Ceram. Technol.*, **16**, 1944 (2019); https://doi.org/10.1111/ijac.13276
18. R.E. El-Shater, A.W. Awad, E.K. Abdel-Khalek, H.H. El-Bahnasawy, T.M. Meaz and E.A. Okba, *Sci. Rep.*, **13**, 15482 (2023); https://doi.org/10.1038/s41598-023-41214-1
19. B. Mahipal, N. Venkatesh, D.R. Kumar and P. Veerasomaiah, *J. Mol. Struct.*, **1277**, 134843 (2023); https://doi.org/10.1016/j.molstruc.2022.134843
20. A.K. Ambala, D.R. Kumar, S.I. Ahmad, K. Anuradha and C.A. Lincoln, *Mater. Today Proc.*, **92(Part 2)**, 801 (2023); https://doi.org/10.1016/j.matpr.2023.04.346
21. B.B.R. Shaikh, B.G. Toksha, S.E. Shirsath, A. Chatterjee, S. Tonde and S.Q. Chishty, *J. Magn. Magn. Mater.*, **537**, 168229 (2021); https://doi.org/10.1016/j.jmmm.2021.168229
22. M. Raghasudha, D. Ravinder and P. Veerasomaiah, *Adv. Mater. Phys. Chem.*, **3**, 89 (2013); https://doi.org/10.4236/ampc.2013.32014
23. K. Pubby, S.S. Meena, S.M. Yusuf and S.B. Narang, *J. Magn. Magn. Mater.*, **466**, 430 (2018); https://doi.org/10.1016/j.jmmm.2018.07.038
24. J. Venturini, A.M. Tonelli, T.B. Wermuth, R.Y.S. Zampiva, S. Arcaro, A.D. Cas Viegas and C.P. Bergmann, *J. Magn. Magn. Mater.*, **482**, 1 (2019); https://doi.org/10.1016/j.jmmm.2019.03.057
25. B. Mahipal, N. Venkatesh, D.R. Kumar and P. Veerasomaiah, *Chem. Zvesti*, **77**, 2839 (2023); https://doi.org/10.1007/s11696-023-02670-1
26. D.D. Andhare, S.R. Patade, J.S. Kounsalye and K.M. Jadhav, *Physica B*, **583**, 412051 (2020); https://doi.org/10.1016/j.physb.2020.412051
27. A.V. Ravindra, M. Chandrika, Ch. Rajesh, P. Kollu, S. Ju and S.D. Ramarao, *Eur. Phys. J. Plus*, **134**, 296 (2019); https://doi.org/10.1140/epjp/i2019-12690-2
28. M.A. Almessiere, Y. Slimani, S. Guner, M. Sertkol, A. Demir Korkmaz, S.E. Shirsath and A. Baykal, *Ultrason. Sonochem.*, **58**, 104654 (2019); https://doi.org/10.1016/j.ultsonch.2019.104654.
29. M. Hashim, M. Raghasudha, S.S. Meena, J. Shah, S.E. Shirsath, S. Kumar, D. Ravinder, P. Bhatt, R. Alimuddin, R. Kumar and R.K. Kotnala, *J. Magn. Magn. Mater.*, **449**, 319 (2018); https://doi.org/10.1016/j.jmmm.2017.10.023
30. X. Jing, M. Guo, Z. Li, C. Qin, Z. Chen, Z. Li and H. Gong, *Ceram. Int.*, **49**, 14046 (2023); https://doi.org/10.1016/j.ceramint.2022.12.286
31. M.A. Almessiere, A.D. Korkmaz, Y. Slimani, M. Nawaz, S. Ali and A. Baykal, *Ceram. Int.*, **45**, 3449 (2019); https://doi.org/10.1016/j.ceramint.2018.10.260
32. G.S. Goud, N. Venkatesh, D.R. Kumar, S.I. Ahmad and P. Veerasomaiah, *ECS J. Solid State Sci. Technol.*, **13**, 073005 (2024); https://doi.org/10.1149/2162-8777/ad5dfb
33. N.M. Reddy, D. Kothandan, V. Poli Reddy, S.R. Juvvala, M.G. Kiran, K.R.R. Chebattina, U.C. Pathem, S.J. Basha, T. Narendrudu and A. Kalpana, *J. Sol-Gel Sci. Technol.*, **113**, 322 (2025).; https://doi.org/10.1007/s10971-024-06602-7
34. S. Balu, D. Ganapathy, S. Arya, R. Atchudan and A.K. Sundramoorthy, *RSC Adv.*, **14**, 14392 (2024); https://doi.org/10.1039/D4RA01307G
35. S. Dabagh, S.A. Haris and Y.N. Ertas, *J. Cluster Sci.*, **34**, 2067 (2023); https://doi.org/10.1007/s10876-022-02373-9
36. S. Kaur, V.K. Chalotra, R. Jasrotia, V. Bhasin, S. Suman, S. Kumari, S. Thakur, J. Ahmed, A. Mehtab, T. Ahmad, R. Singh and S. Godara, *Opt. Mater.*, **133**, 113026 (2022); https://doi.org/10.1016/j.optmat.2022.113026
37. M.A. Sayed, H.K. Abdelsalam and A.A.H. El-Bassuony, *World J. Microbiol. Biotechnol.*, **36**, 25 (2020); https://doi.org/10.1007/s11274-020-2803-x